Journal of Materials Chemistry C

ROYAL SOCIETY OF CHEMISTRY

PAPER

View Article Online
View Journal | View Issue

Cite this: J. Mater. Chem. C, 2024, 12, 7446

High-performance ladder-type conjugated polymer/carbon nanotube nanocomposites blended with elastomers for stretchable thermoelectric thin films†

Qing-Bao Zheng, ‡[a] Chi-Chun Tseng,‡[b] Meng-Hao Lin,[a] Jhih-Min Lin,[c] Shih-Huang Tung,[d] Yen-Ju Cheng *[be] and Cheng-Liang Liu *[af]

Received 1st April 2024,
Accepted 24th April 2024

DOI: 10.1039/d4tc01307g

rsc.li/materials-c

Stretchable thermoelectric thin films have attracted considerable attention due to their prospective applications in wearable electronics. Nevertheless, targeted resolutions are required for persistent challenges such as the increased resistance and diminished electrical conductivity under strain. The present study focuses on the development of high-performance thermoelectric nanocomposites *via* the blending of thienyl–phenylene–thienylene–phenylene–thienyl (TPT) nonacyclic fused ring-based conjugated polymers with single-walled carbon nanotubes (CNTs). To disperse the CNTs, three TPT-based ladder-type random conjugated copolymers featuring distinct acceptor units are investigated, namely (i) thieno[3,4-*c*]pyrrole-4,6(5*H*)-dione (TPD), (ii) diphenylquinoxaline (QX), and (iii) thieno[3,4-*b*]thiophene (TT). Notably, the highly planar backbone structure of TPT–TT efficiently wraps around the surfaces of the CNTs, thus facilitating their uniform dispersion within the nanocomposite film. Consequently, the TPT–TT/CNT nanocomposite exhibits superior thermoelectric properties, including a power factor (PF) of up to 678.8 μW m^{-1} K^{-2}. In addition, stretchable thermoelectric thin films are fabricated on a poly(dimethylsiloxane) (PDMS) substrate by incorporating various amounts of the styrene–ethylene–butylene–styrene (SEBS) elastomer into the TPT–TT/CNT nanocomposite. The ternary TPT–TT/CNT/SEBS25 (containing 25 wt% SEBS) nanocomposite film maintains a PF of 372.79 μW m^{-1} K^{-2} (73.2% of its initial value) at 50% strain. The present study introduces a straightforward approach for fabricating stretchable thermoelectric thin films with commendable thermoelectric performance under strains of up to 50% by blending the high-performance ladder-type conjugated-polymer/CNT nanocomposite with SEBS.

1. Introduction

The contemporary global challenges arising from the combination of energy and environmental concerns have become increasingly pronounced, primarily due to the limited availability of resources and persistent reliance on fossil fuels. This concern is further exacerbated by the burgeoning global population, which has contributed to a marked increase in energy demand. These issues have resulted in a significant surge in interest in renewable energy sources. Meanwhile, a significant amount of waste heat is being generated due to inefficient energy utilization, which is a matter that demands increased scrutiny. Consequently, a great deal of interest has become focused on the development of thermoelectric technology to convert this waste heat into electrical energy in an ecologically conscientious manner.[1–3]

Over the past two decades, extensive research has focused on the development of inorganic semiconductors, especially those based on metal alloys, as promising candidates for thermoelectric materials.[4,5] However, these materials can be excessively costly due to elemental constituents with low natural abundance, and these constituents are often toxic, thereby posing environmental risks.[6] By contrast, organic and hybrid thermoelectric materials have advantages such as abundant constituent elements and low production costs due to their easily scalable room-temperature and solution-processing fabrication methods.[7–11] Moreover, they are lightweight, flexible,

[a] Department of Materials Science and Engineering, National Taiwan University, Taipei 10617, Taiwan. E-mail: liucl@ntu.edu.tw
[b] Department of Applied Chemistry, National Yang Ming Chiao Tung University, Hsinchu 30010, Taiwan. E-mail: yjcheng@nycu.edu.tw
[c] National Synchrotron Radiation Research Center, Hsinchu 30076, Taiwan
[d] Institute of Polymer Science and Engineering, National Taiwan University, Taipei 10617, Taiwan
[e] Center for Emergent Functional Matter Science, National Yang Ming Chiao Tung University, Hsinchu 30010, Taiwan
[f] Advanced Research Center for Green Materials Science and Technology, National Taiwan University, Taipei 10617, Taiwan

† Electronic supplementary information (ESI) available. See DOI: https://doi.org/10.1039/d4tc01307g

‡ These authors contributed equally to this work.

and generally non-toxic.[12,13] Consequently, these materials are currently acknowledged as prominent choices for applications in the field of thermoelectric materials.[14–16]

The efficiency of a thermoelectric device is generally evaluated in terms of the dimensionless figure of merit (ZT), which is given by the following equation:

$$ZT = S^2\sigma T/\kappa \quad (1)$$

where S is the Seebeck coefficient, σ is the electrical conductivity, T is the absolute temperature, and κ is the thermal conductivity.[17] In addition, due to the inherently low thermal conductivity of most polymers, the thermoelectric performance of an organic material is generally evaluated by the power factor (PF):

$$\mathrm{PF} = S^2\sigma \quad (2)$$

While the primary challenge of polymer-based thermoelectric materials has historically revolved around their insufficient electrical conductivity,[18,19] recent progress has been made by incorporating conductive carbon nanofillers such as carbon nanotubes (CNTs) into the polymer matrix.[20–26] These nanocomposites harness the distinctive properties of each constituent to enhance the overall thermoelectric performance.[27,28] Nevertheless, a significant impediment in the development of these nanocomposites lies in effective regulation of the dispersion of CNTs within the polymer nanocomposite.[29–31] The strong surface energy and mutual attraction among CNTs *via* van der Waals forces often lead to the formation of self-aggregated CNT bundles. Consequently, it is imperative to design novel conducting polymers for integration into thermoelectric nanocomposite materials.[32,33] To address this need, donor–acceptor (D–A) conjugated polymers are regarded as more promising candidates due to their stronger intermolecular interaction forces and highly planar backbone structures.[34–36] For example, Jung *et al.* fabricated thermoelectric nanocomposite films comprising a cyclopentadithiophene (CDT)-based D–A conjugated polymer and CNTs to achieve a PF of up to 459 μW m^{-1} K^{-2}.[37] Meanwhile, Kim *et al.* presented a nanocomposite film incorporating the ladder-type indacenodithiophene-*co*-benzothiadiazole (IDTBT) polymer and CNTs to achieve remarkable electrical conductivity and PF values of 853.5 S cm^{-1} and 697 μW m^{-1} K^{-2}, respectively. The increased electrical conductivity was attributed to the highly planar IDTBT backbone, which enhanced the efficiency of intramolecular charge transport at the inter-CNT junctions.[25] The aforementioned studies also highlighted the significant potential of D–A conjugated polymers with highly planar backbone structures for achieving stable dispersion and efficient debundling of the CNTs. This capability holds promise for achieving high thermoelectric performance in the resulting nanocomposites.[38]

Recent advances in stretchable electronics have opened up new frontiers for diverse applications such as stretchable light-emitting diodes,[39] soft batteries,[40] stretchable sensors,[41] and supercapacitors,[42] which play important roles in establishing versatile connections between humans and machines by enabling the evolution of wearable and implantable electronic devices.[11,43–45] However, the mechanical properties and stretchability of CNT-based thermoelectric composites face inherent limitations arising from intrinsic brittleness of CNTs, making them susceptible to deformation under tensile strain and mechanical stress. Consequently, contemporary research initiatives have been progressively focused on refining the incorporation of additional stretchable materials and the design of the device configuration of CNT-based thermoelectric devices, with the aim of increasing their overall stretchability.[46] For example, Zhang *et al.* employed a modified wet-spinning method to fabricate stretchable thermoelectric fibers. These fibers were gradually extruded from a CNT solution into a coagulation bath comprising waterborne polyurethane (WPU) and poly(vinyl) alcohol (PVA). The resulting annealed thermoelectric fibers exhibited a Seebeck coefficient of 44 μV K^{-1} and a PF of 1.78 μW m^{-1} K^{-2} at room temperature. Remarkably, even under a 20% tensile strain, the Seebeck coefficient remained nearly constant, with only a slight increase in resistance.[47] Meanwhile, He *et al.* prepared the poly(3,4-ethylenedioxythiophene): poly(styrenesulfonate) (PEDOT:PSS)/CNT composite films onto electrospun polyurethane (PU)/polycaprolactone (PCL) nanofiber films using a vacuum filtration method followed by hot pressing. The resulting composite films exhibit a PF of 1.9 μW m^{-1} K^{-2} and stretching strain of more than 400%.[48] Liang *et al.* reported stretchable thermoelectric films of polypyrrole (PPy)/CNT composites using a common vacuum filtration method. The corresponding conductivity and PF for the PPy/CNT composite films can be achieved at approximately 20 μW m^{-1} K^{-2} and stretched up to 3.2%.[49] While the aforementioned studies have achieved success in the production of stretchable thermoelectric composites based on CNTs, there persist challenges in the actualization of wearable devices. For these devices to be considered viable for wearable applications, they necessitate the manifestation of elevated thermoelectric properties when subjected to external strains, given the crucial role of mechanical resilience in practical applications. Consequently, this emphasizes the imperative for additional research efforts aimed at developing stretchable CNT-based thermoelectric composites that can effectively retain their high-performance thermoelectric properties under varying strains.

In the present study, a straightforward approach is presented in which D–A random conjugated polymers based on the ladder-type thienyl–phenylene–thienylene–phenylene–thienyl (TPT) nonacyclic fused ring are blended with CNTs and strategically combined with the elastic polymer styrene–ethylene–butylene–styrene (SEBS) to obtain a highly stretchable thermoelectric thin film. To systematically investigate the impact of the planar chemical structure on the dispersity and doping effect of the CNTs, various acceptor units, including thieno[3,4-*c*]pyrrole-4,6(5*H*)-dione (TPD), diphenylquinoxaline (QX), and thieno[3,4-*b*]thiophene (TT), are introduced into the TPT-based conjugated polymers to obtain the samples designated as TPT–TPD, TPT–QX, and TPT–TT, respectively. Subsequently, the optimal TPT–TT/CNT nanocomposite is combined with the optimal amount (25 wt%) of SEBS in order to impart elastic properties to the nanocomposite, enabling the fabrication of stretchable thermoelectric films. When applied to a PDMS substrate, the resulting TPT–TT/CNT/SEBS25 ternary

nanocomposite exhibits a noteworthy PF value of 372.8 μW m^{-1} K^{-2} under a 50% strain, maintaining 73.2% efficacy compared to the unstrained state. Thus, the present study provides a novel methodology for the fabrication of stretchable thermoelectric nanocomposite thin films that exhibit exceptional thermoelectric performances even under strains of up to 50%, thereby paving the way for potential applications in wearable electronics and energy harvesting.[43,50,51]

2. Experimental section

2.1. Materials

The solvents 1,2-dichlorobenzene (*o*-DCB, anhydrous, 99%), chlorobenzene (CB, anhydrous, 99.8%), and isopropanol (IPA), along with the styrene–ethylene–butylene–styrene (SEBS) thermoplastic elastomer, were purchased from Sigma-Aldrich. The TuballTM single-walled carbon nanotubes (SWCNTs) with a purity of approximately 85% were acquired from OCSiAl. All chemicals and solvents were used as received and without further purification.

2.2. Preparation of the D–A polymers

According to our previous report,[52] Stille copolymerization was used to combine the dibrominated nonacylic thienyl–phenylene–thienylene–phenylene–thienyl (TPT) with various acceptor units: thieno[3,4-*c*]pyrrole-4,6(5*H*)-dione (TPD), diphenylquinoxaline (QX), and thieno[3,4-*b*]thiophene (TT). The resulting ladder-type D–A random conjugated copolymers, with a molar ratio of 1 : 1, are denoted hereafter as the TPT–TPD, TPD–QX, and TPD–TT, respectively, and their chemical structures are shown in Fig. 1a. These were used to investigate the effect of the planar chemical structure on the dispersity of the CNTs and on the subsequent thermoelectric performance of the nanocomposite. The molecular weights, polydispersity index, and thermal properties of TPT-based conjugated polymers results are summarized in Table S1 (ESI†).

2.3. Fabrication of the thermoelectric thin films

The fabrication of the various polymer/CNT and polymer/CNT/SEBS thermoelectric thin films is shown schematically in Fig. 1b. First, the D–A copolymer was dissolved in *o*-DCB at a concentration of 0.5 mg mL^{-1}, and the mixture was stirred at 70 °C for 6 h to achieve complete dissolution. An equivalent amount of CNTs was then introduced into the polymer solution to obtain a total solid content of 1 mg mL^{-1}. To ensure a homogeneous blend, the nanocomposite solution was thoroughly mixed using a ball mill (Restch MM440) at 30 Hz for 15 min. After that, SEBS was dissolved in *o*-DCB and added to the homogeneous solutions of nanocomposites in various nanocomposite : SEBS ratios (100 : 0, 75 : 25, 50 : 50), in order to optimize the trade-off between the stretchability and thermoelectric properties.[53] In the case of TPT–TT/CNT-based nanocomposites blended with SEBS, the samples were designated as the TPT–TT/CNT/SEBS25, TPT–TT/CNT/SEBS50, and TPT–TT/CNT/SEBS75 for 25, 50, and 75 wt%, respectively.

Prior to use, the glass substrates were cleaned thoroughly *via* sequential ultrasonication in deionized water, acetone, and isopropanol for 10 min each, and then meticulously dried. After that, the glass substrates were subjected to additional cleaning by UV/O_3-treatment. The nanocomposite films were then fabricated on the glass substrates by spin coating at 1000 rpm for 15 s. The resulting films with a size of 1.5 × 0.75 cm were then annealed at 190 °C for 15 min, followed by cooling to room temperature, in a N_2-filled glove box. The resulting nanocomposite thin films exhibited smooth surfaces, with a thickness of approximately 200 nm, as determined by using an Alpha-Step® D-300 surface profiler (KLA-Tencor).

For the stretchable substrate, a PDMS slab was prepared by casting a standard mixture consisting of 10 parts base

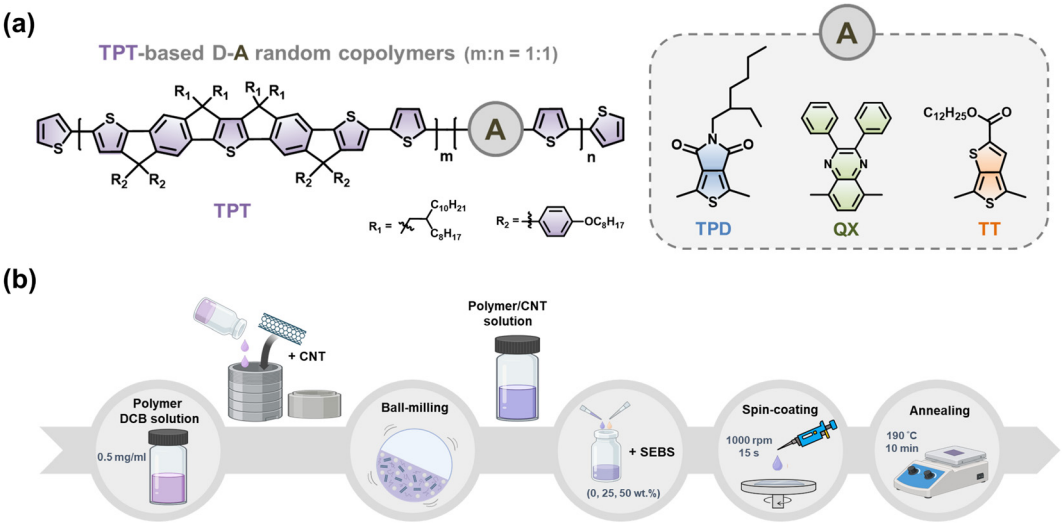

Fig. 1 (a) The chemical structures of the TPT-based ladder-type conjugated copolymers. (b) A schematic diagram showing the preparation of the TPT-based conjugated polymer/CNT nanocomposite films blended with SEBS.

elastomer and 1 part curing agent. To eliminate any trapped air bubbles, the mixing container was subjected to vacuum conditions for 25 min and subsequently cured in an oven at 60 °C for 24 h. To remove any surface contaminants and activate the surface for deposition of the polymer films, the PDMS was then immersed in CB for 30 s, followed by a brief dip in IPA. After that, the nanocomposite films were spin-coated onto the PDMS substrate by using the same procedure as that for the glass substrates.[54] The resulting stretching films (1.5 × 0.75 cm) were also smooth and approximately 200 nm in thickness.

3. Results and discussion

The ladder-type D–A random conjugated copolymers, with a molar ratio of 1 : 1, are denoted as the TPT–TPD, TPT–QX, and TPT–TT, respectively, and their chemical structures are shown in Fig. 1a. These were used to investigate the effect of the planar chemical structure on the dispersity of the CNTs and on the subsequent thermoelectric performance of the nanocomposite. Moreover, the fabrication of the various polymer/CNT and polymer/CNT/SEBS thermoelectric thin films is shown schematically in Fig. 1b. The D–A conjugated polymers were designed to achieve the effective debundling and electrical percolation of the CNTs within the polymer/CNT nanocomposites *via* strong π–π interactions, which are supported by an enhanced polymer backbone planarity. To elucidate the optimal conformation of the polymer backbone, DFT calculations were first performed at the B3LYP/6-311G** level based on one repeating unit of the TPT-based ladder-type conjugated polymer. For computational simplicity, the intricate alkyl side chains were replaced with methyl/ethyl groups in the model compound. The optimized configuration of this simplified model compound is depicted in Fig. S1 and S2 (ESI†). The computational results reveal an exceptionally small dihedral angle of 0.17–0.33° within the ladder-type moieties of the TPT-based copolymers, thereby indicating an extraordinarily coplanar backbone. Moreover, in the case of the TPT-TT, the planarity is expected to be further enhanced due to the smaller dihedral angle between the thiophene units of the polymer backbone and those of the acceptor molecule relative to those of the other two acceptors. Based on previous studies,[55,56] the quinoidization of the TT moiety has been shown to increase the extent of conjugation length and induce coplanarity effects in the polymer backbone. By contrast, the larger dihedral angle between the thiophene units of the polymer backbone and those of the QX can be attributed to steric hindrance by the six-membered rings.

Previous studies have demonstrated that the high electrical conductivity of the CNTs and the superior Seebeck coefficient of the conjugated polymers can be combined to achieve a delicate balance in the nanocomposite material. Hence, the thermoelectric characteristics of the binary TPT–TPD/CNT, TPT–QX/CNT, and TPT–TT/CNT nanocomposites are shown in Fig. 2. Here, all the nanocomposite films exhibit positive Seebeck coefficients, thereby indicating p-type thermoelectric behavior in which holes serve as the primary charge carriers. Moreover, the as-fabricated nanocomposite films exhibit consistently high Seebeck coefficients of ~70 μV K^{-1}, which are superior to those of the most polythiophene-based materials and other D–A copolymers, as illustrated in Fig. S3 (ESI†). The results also indicate that the thermoelectric performance of the nanocomposite is predominantly influenced by the electrical conductivity. Notably, along with its Seebeck coefficient of 69.9 μV K^{-1}, the TPT–TT/CNT nanocomposite film exhibits the highest electrical conductivity and PF of 1390.4 S cm^{-1} and 678.8 μW m^{-1} K^{-2}, respectively. As shown in Fig. S4 (ESI†), the PF of this nanocomposite is superior to that observed in other D–A polymer/CNT nanocomposite films. This result indicates that the optimum thermoelectric properties are obtained for the composite with the highest level of structural planarity, in agreement with the results derived from DFT calculations.

Moreover, the charge-carrier mobility (μ) in each binary nanocomposite film is quantified by the Hall effect measurements in Table S2 (ESI†). Thus, despite minimal differences in carrier concentration (n) among the three nanocomposites (which is due to their identical polymer : CNT weight ratios of 1 : 1), the charge-carrier

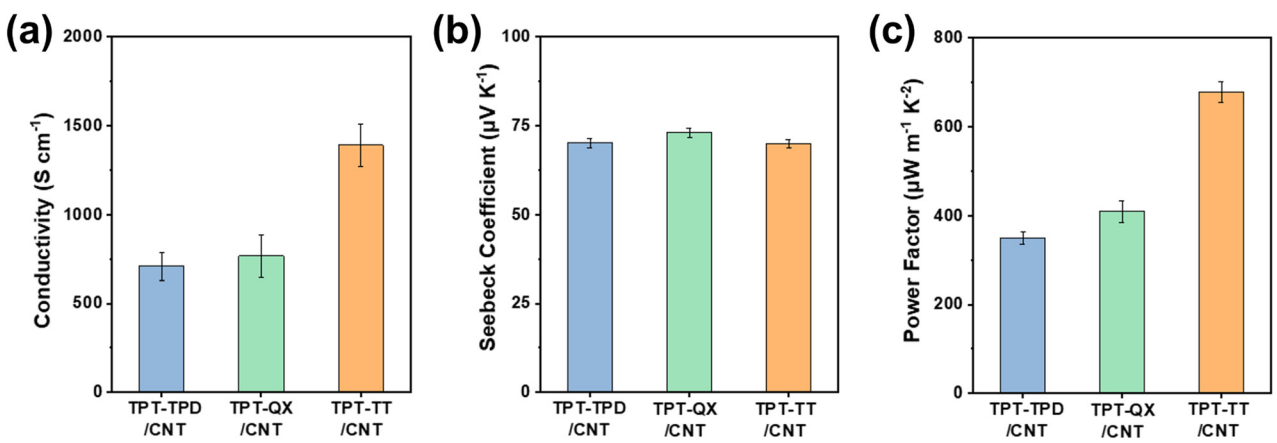

Fig. 2 (a) Electrical conductivity, (b) Seebeck coefficient, and (c) PF of the binary TPT–TPD/CNT, TPT–QX/CNT, and TPT–TT/CNT nanocomposites at 303 K.

mobility of the TPD–TT/CNT nanocomposite (0.37 $cm^2 V^{-1} s^{-1}$) is significantly higher than those of the TPT–TPD (0.18 $cm^2 V^{-1} s^{-1}$) and TPT–QX (0.21 $cm^2 V^{-1} s^{-1}$) nanocomposites.

The UV-vis absorption spectra of the various nanocomposites with and without CNTs are presented in Fig. 3(a–c), while the PL spectra are presented in Fig. 3(d–f). Thus, each material exhibits a distinct UV-vis absorption peak within the 300–650 nm range, which is attributed to the π–π* transitions of the polymer backbone. Notably, these peaks become broader and exhibit red-shifts of approximately 25–40 nm after addition of the CNTs. Moreover, the TPT–TT/CNT film exhibits the most substantial red-shift (Fig. 3(c)), thereby indicating that the strongest π–π interactions exist between the TPT–TT and the CNTs. This can be attributed to the fewer twisted conformations present in the conjugated backbone of the TPT–TT, in agreement with the abovementioned DFT calculations. Meanwhile, the PL spectra of the TPT–TPD, TPT–QX, and TPT–TT nanocomposite solutions indicate PL quenching efficiency (PLQE) values of 62.4%, 72.7%, and 82.4%, respectively.[57,58] This indicates that the incorporation of CNTs into the polymer leads to the quenching of the PL spectrum, with the maximum extent of quenching occurring for the TPT–TT/CNT nanocomposite. Thus, both the UV-vis and PL spectra demonstrate stronger π–π interactions between the CNTs and TPT–TT, which can be attributed to the coplanar structure of TPT–TT. This structural feature results in a greater extent of the polymer wrapping around the surfaces of the CNTs. Notably, the observed trend in the PLQE value corresponds to that observed in the thermoelectric performance, thereby emphasizing the significance of the PLQE as an important indicator of the degree of interaction between the polymer and CNTs in the nanocomposites.

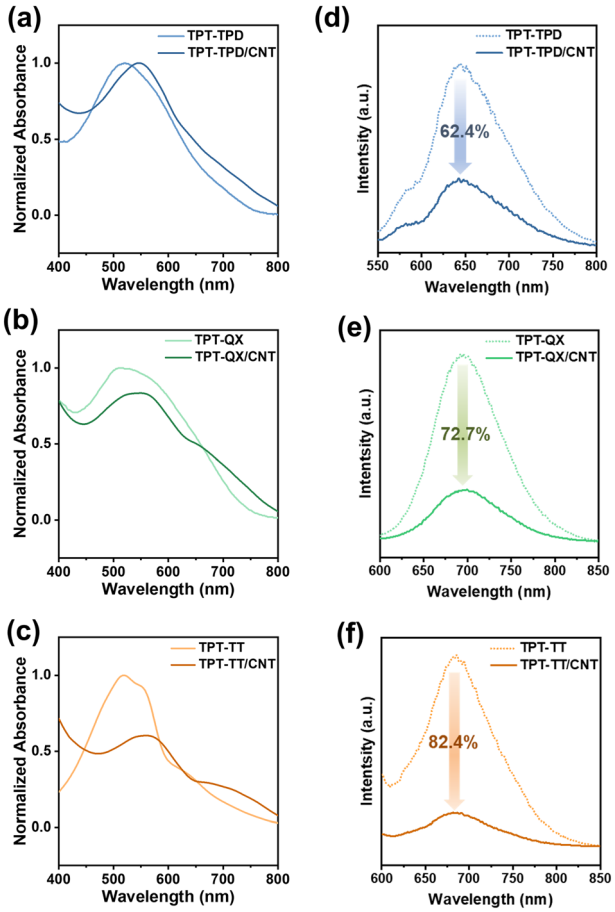

Fig. 3 Normalized UV-vis absorption and PL spectra for the diluted solution of (a) and (d) TPT–TPD and TPT–TPD/CNT, (b) and (e) TPT–QX and TPT–QX/CNT, (c) and (f) TPT–TT and TPT–TT/CNT.

The Raman spectra of the TPT–TPD, TPT–QX, and TPT–TT polymers with and without CNTs are presented in Fig. S5 (ESI†), along with that of the pristine CNTs. There, the pristine CNTs exhibit characteristic Raman peaks at 1572 and 1593 cm^{-1} (termed the G^+ and G^- bands, respectively) due to the in-plane vibrations of the sp^2 hybridized carbon atoms, along with a peak at 1362 cm^{-1} (termed the D band) due to disorder-induced resonance scattering. In addition, a peak is observed in the radial breathing mode (RBM) region of the Raman spectrum (spanning from 100 to 400 cm^{-1}) due to vibrational motions of the CNTs (left-hand panels, Fig. S5, ESI†). By contrast, all three binary nanocomposite films display prominently low D bands and high G/D band ratios, along with a significant reduction in the RBM peaks, thereby indicating the absence of significant structural defects and the inhibition of the CNT vibrations due to wrapping by the polymer chains. Meanwhile, the Raman spectra of the pristine polymers and the polymer/CNT composites each exhibit distinct peaks due to the stretching vibrations of the C–C and C=C bonds in the thiophene rings, along with the S–C bonds of the TPT-based copolymer backbones. Moreover, the thiophene-ring C–C and C=C peaks exhibit redshifts of approximately 2–6 cm^{-1} upon introduction of the CNTs into the copolymers, due to the strong π–π interactions between TPT-based conjugated polymers and the CNTs. Taken together, these results demonstrate the successful syntheses of the polymer/CNT nanocomposites.

In a previous study, the highest occupied molecular orbital (HOMO) energy levels of pristine SWCNTs and the pristine TPT–TPD, TPT–QX, and TPT–TT copolymers were reported as −5.10, −5.20, −5.27, and −5.22 eV, respectively.[52] Based on those results, a relative energy-level diagram for the interface between the TPT-based conjugated copolymers and the CNTs is presented in Fig. S6(a) (ESI†). Notably, all three TPT-based conjugated copolymers exhibit sufficiently similar HOMO levels to that of the pristine SWCNTs, thereby facilitating effective interaction at the interfaces.

The interactions between the TPT-based conjugated polymers and the CNTs are further elucidated by the UPS results in Fig. S6(b) (ESI†). Here, the work function (W_F) values of the pristine CNTs and the TPT–TPD/CNT, TPT–QX/CNT, and TPT–TT/CNT nanocomposite films are 4.44, 4.68, 4.71, and 4.88 eV, respectively. This increase in W_F upon addition of the TPT-based conjugated copolymers to the CNTs suggests that the TPT-based conjugated copolymers function as p-type dopants, effectively shifting the W_F towards the HOMO energy levels.[59] Moreover, the W_F increases in the order of

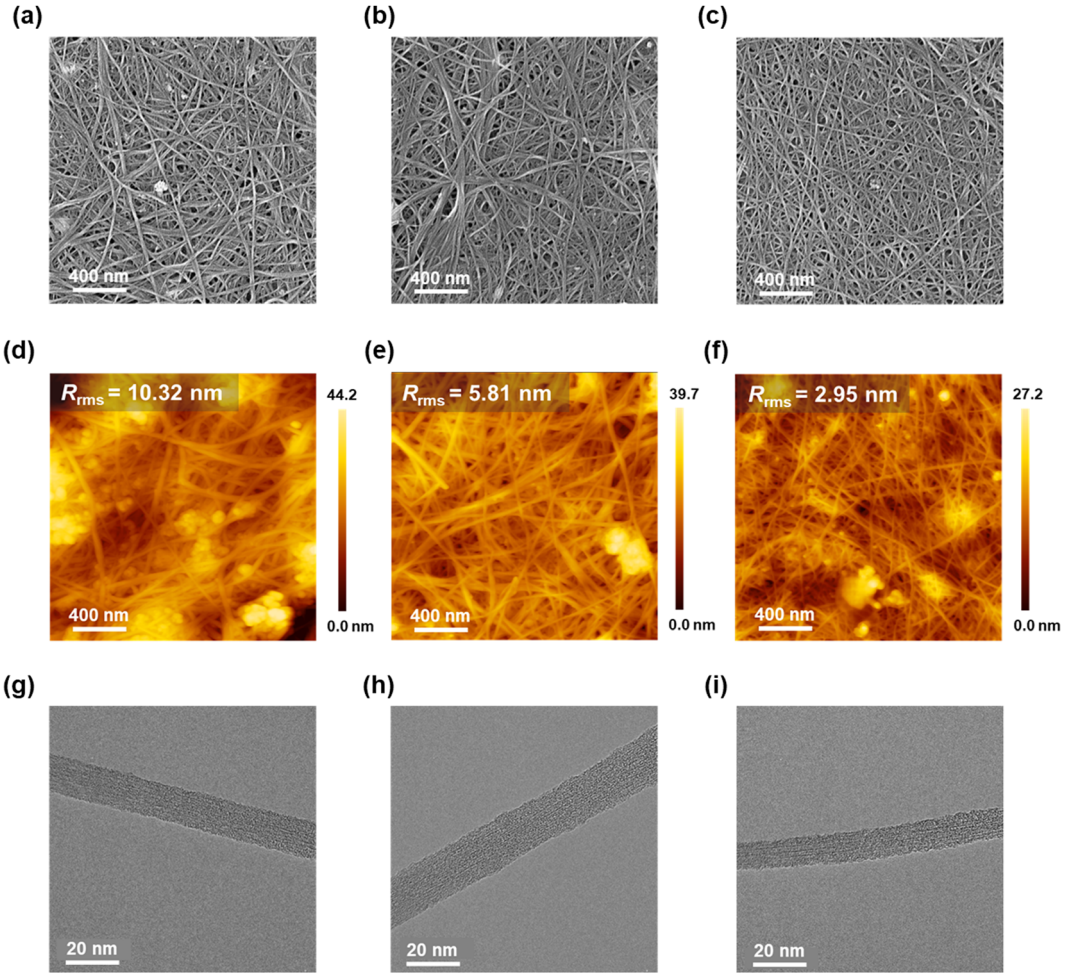

Fig. 4 (a)–(c) SEM, (d)–(f) AFM, and (g)–(i) TEM images of the (a), (d) and (g) TPT–TPD/CNT, (b), (e) and (h) TPT–QX/CNT, and (c), (f) and (i) TPT–TT/CNT nanocomposites measured at 303 K. (d) Photographic image showing the TT/CNT/SEBS25 film under 0% (top) and 50% (bottom) strains. Electrical conductivity, Seebeck coefficient, and PF values for the (e) and (f) TPT–TT/CNT/SEBS25 and the (g) and (h) TPT–TT/CNT/SEBS50 under strains of 0–50%.

CNT < TPT–TPD/CNT < TPT–QX/CNT < TPT–TT/CNT, thereby indicating a higher doping level for the TPT–TT/CNT nanocomposite films. This trend is consistent with the observed thermoelectric performance, thereby demonstrating the influence of the polymer doping level on the overall thermoelectric characteristics of the nanocomposite system.

The surface morphologies of the various binary nanocomposite films are revealed by the SEM, AFM, and TEM images in Fig. 4. Here, distinctly entangled CNT bundles and pore spaces are evident in the SEM images of the TPT–TPD/CNT and TPT–QX/CNT films (Fig. 4(a and b)), due to van der Waals forces between the CNTs. This will inevitably result in a decrease in the number of electrical junctions. By contrast, the TPT–TT/CNT nanocomposite film exhibits a slight reduction in pinhole density and CNT-bundle diameter (Fig. 4(c)), thereby indicating that the planar TPT-TT efficiently wraps around the surface of the CNTs, thus leading to the uniform dispersion of CNTs within the nanocomposite film. Furthermore, the AFM images in Fig. 4(d–f) clearly indicate the tendency of the CNTs to self-aggregate within the TPT–TPD polymers, thus resulting in an uneven distribution and surface roughness. Notably, the root-mean-square surface roughness (R_{rms}) is seen to decrease significantly in the following sequence: TPT–TPD/CNT (10.32 nm) > TPT–QX/CNT (5.81 nm) > TPT–TT/CNT (2.95 nm). This indicates a substantial reduction in bundle size due to the enhanced π–π interactions between the planar-shaped TPT–TT and the CNTs, which reduce the interstitial spacing between the CNTs to result in a significantly more compact TPT–TT/CNT nanocomposite film.

The polymer wrapping around one isolated CNT bundle is revealed by the TEM images in Fig. 4(g–i). Notably, the diameters of the wrapped CNT bundles range between 10 and 15 nm depending on the specific polymer in the nanocomposite. Thus, while the TPT–TPD and TPT–QX exhibit less extensive wrapping around the CNTs, the highly planar backbone geometry of the TPT–TT allows it to adhere tightly to the outer surfaces of the CNTs *via* weak non-covalent (π–π) interactions. The resulting increase in polymer coverage on the CNT surface may explain the improved dispersion and smaller size of the CNT bundles. This, in turn, may have resulted in the establishment of a more effective electrical conduction pathway, as evidenced by the Hall effect measurements. Thus, the high

carrier mobility of the TPD–TT/CNT can be attributed to the increased conducting cross-section (*via* stronger π–π interfacial interactions) and correspondingly decreased resistivity of the intra-tube junctions between adjacent CNTs. These observations suggest that the TPT–TT effectively reduces the tendency of the CNTs to aggregate, thereby establishing a favorably interconnected and electrically conductive CNT network.

The microstructures of the pristine polymers and the binary polymer/CNT nanocomposites are further revealed by the GIWAXS results in Fig. S7 and S8 (ESI†). Thus, before the addition of CNTs, the GIWAXS patterns of the pristine TPT-based conjugated polymers exhibit broad, diffuse rings that are indicative of predominantly amorphous structures, with no discernible crystallinity (Fig. S7(a–c), ESI†). After the addition of CNTs, however a characteristic diffraction ring appears at $q \approx 2.1$ Å^{-1} due to the presence of CNTs within the nanocomposites (Fig. S7(d–f), ESI†). Moreover, the conjugated polymer/CNT nanocomposites exhibit new π–π stack peaks in the out-of-plane direction at $q_z \approx 1.55$ Å^{-1}, thereby indicating that the addition of CNTs induces a rearrangement of the conjugated polymer chains and the formation of a new microstructure embedded with CNTs.

The effects of various amounts of SEBS (0, 25, and 50 wt%) on the thermoelectric properties of the TPT–TPD/CNT, TPT–QX/CNT, and TPT–TT/CNT nanocomposites are revealed in Fig. 5(a–c). Notably, as with the binary nanocomposite films, the variation in thermoelectric performance with the addition of SEBS is predominantly driven by the variation in electrical conductivity. Specifically, due to its insulating nature, the incorporation of SEBS leads to a reduction in electrical conductivity (Fig. 5(a)) while having relatively little effect on the Seebeck coefficient (Fig. 5(b)).[60] Consequently, although a sample was prepared using 75 wt% SEBS, the electrical resistances of the resulting polymer/CNT/SEBS75 films were too high for measurement. Meanwhile, the PF values of the composites are seen to decrease with the addition of 25 wt% and 50 wt% SEBS, respectively (Fig. 5(c)). Moreover, the optimum effect on thermoelectric performance is observed for the TPT–TT/CNT-based system. Therefore, the TPT–TT/CNT/SEBS25 and TPT–TT/CNT/SEBS50 nanocomposites that were spin-coated onto soft PDMS substrates were subjected to various strain levels (0–50%) and their corresponding thermoelectric performances are shown in Fig. 5(e–h), while photographic images of the TPT–TT/CNT/SEBS25 film before and after stretching are shown in Fig. 5(d). Thus, the TPT–TT/CNT/SEBS25 nanocomposite exhibits an electrical conductivity of 771.5 S cm^{-1} and a Seebeck coefficient of 69.5 μV K^{-1} at 50% strain (Fig. 5(e)), along with a PF of 372.8 μW m^{-1} K^{-2}, which represents a 73.2% retention relative to that in the unstretched state (PF/PF$_0$) (Fig. 5(f)). Meanwhile, the TPT–TT/CNT/SEBS50 nanocomposite exhibits an electrical conductivity and a Seebeck coefficient of 386.1 S cm^{-1} and 68.7 μV K^{-1}, respectively, at 50% strain (Fig. 5(g)), along with a PF of 181.9 μW m^{-1} K^{-2}, indicating a 80.6% retention relative to the unstretched state (Fig. 5(h)). In brief, these results indicate that the conductivity decreases, while the Seebeck coefficient increases slightly, as the strain level is increased. Furthermore, the decline in the PF with increasing strain is consistent with the trend in conductivity, as the conductivity plays a more dominant role than the Seebeck coefficient. Moreover, a comparison of Fig. 5(f–h) indicates that the PF of the TPT–TT/CNT/SEBS50 nanocomposite film decreases more slowly than that of the TPT–TT/CNT/SEBS25 with the increase in the strain level. This may be attributed to the higher proportion of the SEBS elastomer, which enhances the stretchability of the thermoelectric film. At higher strains (*e.g.* 75%), however, the resistances of the nanocomposite films exceeded the measurable range. Nevertheless, as demonstrated in Fig. S3 and S4 (ESI†), the thermoelectric properties of the ternary nanocomposite films developed herein surpass those of the previously reported

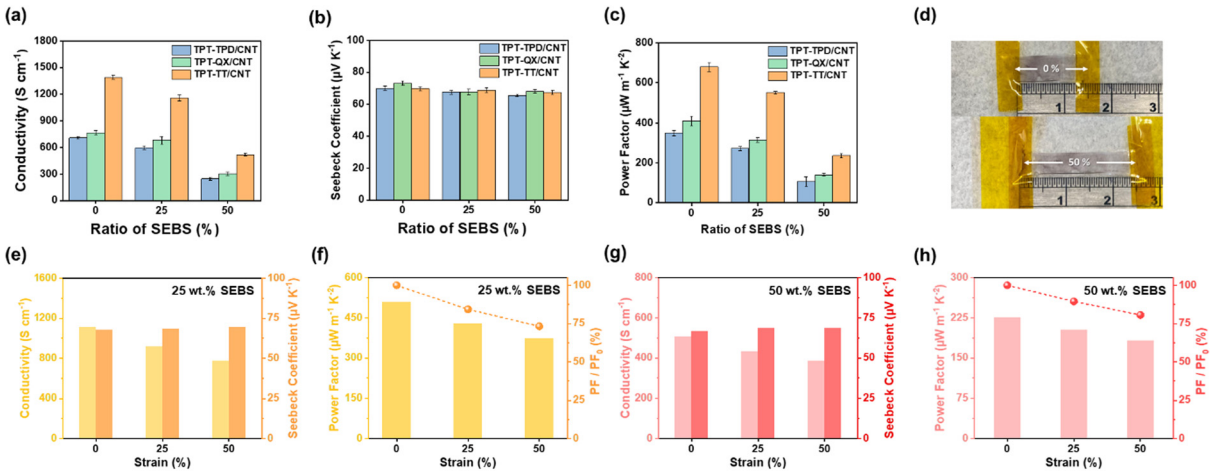

Fig. 5 (a) Electrical conductivity, (b) Seebeck coefficients, and (c) PF values of the TPT–TPD/CNT, TPT–QX/CNT, and TPT–TT/CNT nanocomposites with 0, 25, and 50 wt% SEBS (values measured at 303 K). (d) Photographic image showing the TT/CNT/SEBS25 film under 0% (top) and 50% (bottom) strains. Electrical conductivity, Seebeck coefficient, and PF values for the (e) and (f) TPT–TT/CNT/SEBS25 and the (g) and (h) TPT–TT/CNT/SEBS50 under strains of 0–50%.

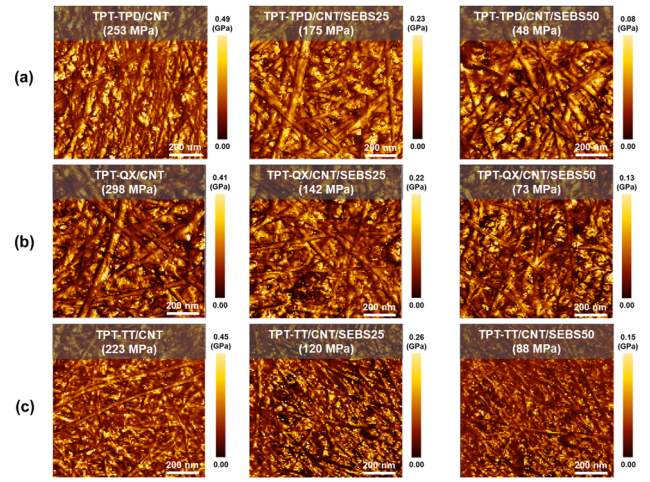

Fig. 6 The DMT modulus maps of the (a) TPT–TPD/CNT, (b) TPT–QX/CNT and (c) TPT–TT/CNT nanocomposite films with the addition of 25 wt% (middle) and 50 wt% SEBS (right).

conjugated polymer/CNT nanocomposite systems, even with the addition of the insulating elastomers, thereby demonstrating the potential of the TPT–TT/CNT/SEBS system for the fabrication of stretchable thermoelectric thin films.

The DMT maps of the TPT–TPD/CNT, TPT–QX/CNT and TPT–TT/CNT nanocomposite films with various polymer/CNT:SEBS weight ratios (100 : 0, 75 : 25, and 50 : 50) are presented in Fig. 6. Thus, in the absence of SEBS, the dispersion of CNT bundles in the various binary copolymer/CNT nanocomposites is similar to that observed in Fig. 4(a–c), while the elastic moduli of the three binary nanocomposites are seen to be approximately 253, 298, and 223 MPa, respectively (left-hand column, Fig. 6). Moreover, with the addition of 25 wt% SEBS, the dispersion of CNT bundles is largely unaffected, while the elastic moduli are reduced to almost half their initial values, becoming 175, 142, and 120 MPa, respectively (middle column, Fig. 6). This represents a significant enhancement in the deformability and stretchability of each nanocomposite without significantly affecting the morphology of the polymer/CNT nanocomposites.[61] This can be attributed to the formation of entangled, amorphous, flexible SEBS domains within each film. These domains can dissipate the strain energy and protect the rigid polymer/CNT nanocomposite from damage under strain.[62] This is further supported by the results in the right-hand column of Fig. 6, where the addition of 50 wt% SEBS leads to elastic moduli of 48, 73, and 88 MPa for the TPT–TPD/CNT–, TPT–QX/CNT– and TPT–TT/CNT-based films, respectively. In brief, these results indicate a substantial enhancement in the ductility of each polymer/CNT film due to the incorporation of SEBS into the nanocomposite. Moreover, the greatest improvement is observed for the TPT–TT/CNT-based nanocomposite.

The surface structures of the binary TPT–TT/CNT and ternary TPT–TT/CNT/SEBS25 and TPT–TT/CNT/SEBS50 nanocomposites under mechanical strains of 0–75% are revealed by the optical microscope images in Fig. 7. Here, a significant number of cracks, on the scale of several hundreds of microns, appear on the binary TPT–TT/CNT nanocomposite film upon the application of 25% strain, and these are oriented more-or-less parallel to the direction of strain. By contrast, no cracks are observed on the two ternary nanocomposite films at 25% strain, and only a few cracks appear at 50% strain. Moreover, these cracks are oriented perpendicular to the direction of strain, thus suggesting a substantial enhancement in the ductility of the TPT–TT/CNT/SEBS films due to the incorporation of SEBS. In addition, the ternary TPT–TT/CNT/SEBS50 nanocomposite thin film exhibits greater strain resistance than TPT–TT/CNT/SEBS25, exhibiting only very minor cracking at 50% strain. Moreover, while a slight imbalance between the improved stretchability and the thermoelectric properties is indicated by the decrease in electrical conductivity in Fig. 5(e–g), the better-preserved microstructures and limited cracking of the ternary TPT–TT/CNT/SEBS25 and TPT–TT/CNT/SEBS50 nanocomposite films undoubtedly help to maintain their conductivity.

Taken together, these results indicate that the addition of SEBS both enhances the mechanical endurance and maintains the thermoelectric properties of the ternary thin films. In

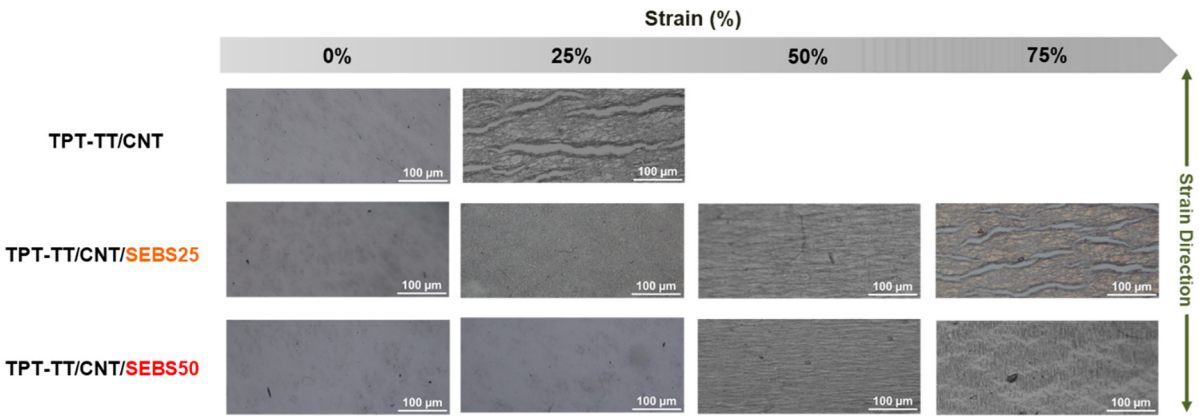

Fig. 7 Optical microscope images of the TPT–TT/CNT (top), TPT–TT/CNT/SEBS25 (middle), and TPT–TT/CNT/SEBS50 (bottom) nanocomposite films under strains of 0–75%. The scale bars all represent 100 μm.

particular, the excellent thermoelectric performance of the TPT–TT/CNT/SEBS25 film, combined with its ability to withstand stress, indicates a good balance between stretchability and excellent thermoelectric properties. As a further demonstration, the thermoelectric properties of the ternary TPT–TT/CNT/SEBS25 thin film on a PDMS substrate were stretched in air for 250 stretching/releasing cycles of stretching to 25% strain and measured by the ZEM-3 instrument to track the thermoelectric parameters including Seebeck coefficient and conductivity are presented in Fig. S9 (ESI†). Here, the TPT–TT/CNT/SEBS25 thin film exhibits PF retentions of 82.8% and 71.9% after 150 and 250 cycles, respectively, relative to its initial state, thereby demonstrating excellent cyclic stability. In summary, the above report introduces a novel approach to the creation of stretchable thermoelectric thin films with potential applications in wearable thermoelectric generators by dispersing CNTs in ladder-type conjugated polymers and introducing the SEBS elastomer to provide a balance between the stretchability and thermoelectric performance.

4. Conclusions

Herein, high-performance thermoelectric thin films were fabricated by dispersing carbon nanotubes (CNTs) in ladder-like thienyl–phenylene–thienylene–phenylene–thienyl (TPT)-based donor–acceptor (D–A) conjugated copolymers. In addition, the elastomer styrene–ethylene–butylene–styrene (SEBS) was incorporated in order to fabricate stretchable thermoelectric thin films. Three different acceptors were investigated, and thieno[3,4-*b*]thiophene (TT) was found to give the best results, providing a binary TPT–TT/CNT nanocomposite with a commendable Seebeck coefficient and conductivity of $\sim$70 μV K^{-1} and 1390.4 S cm^{-1}, respectively, along with a superior power factor (PF) of 678.8 μW m^{-1} K^{-2} relative to other D–A conjugated polymer/CNT-based nanocomposite films. Furthermore, the incorporation of SEBS successfully enhanced the stretchability of the TPT–TT/CNT nanocomposite system, such that the ternary TPT–TT/CNT/SEBS25 nanocomposite exhibited a 73.2% PF retention under a strain of 50%. Our results present a new route for fabricating a high-performance polymer/CNT composite thermoelectric thin film capable of withstanding a 50% strain while simultaneously exhibiting a commendable thermoelectric performance, with potential applications in wearable thermoelectric generators.

Conflicts of interest

There are no conflicts to declare.

Acknowledgements

The authors acknowledge financial support from the 2030 Cross-Generation Young Scholars Program by the National Science and Technology Council (NSTC) in Taiwan under grants 112-2628-E-002-013 and 112-2221-EA49-002, the Academic Research-Career Development Project (Sprout Research Projects) by National Taiwan University (NTU112L7856), and the Advanced Research Center for Green Materials Science and Technology from The Featured Area Research Center Program within the framework of the Higher Education Sprout Project by the Ministry of Education (112L9006). The authors also thank Beamline TPS 25A at the National Synchrotron Radiation Research Center (NSRRC) of Taiwan for providing beamtime and Ms C.-Y. Chien and S.-J. Ji for assistance with FE-TEM and SEM experiments of the Instrumentation Center at National Taiwan University which is supported by the NSTC in Taiwan.

Notes and references

1 R. Kroon, D. A. Mengistie, D. Kiefer, J. Hynynen, J. D. Ryan, L. Yu and C. Muller, *Chem. Soc. Rev.*, 2016, **45**, 6147.
2 L. Zhang, X.-L. Shi, Y.-L. Yang and Z.-G. Chen, *Mater. Today*, 2021, **46**, 62.
3 M. Massetti, F. Jiao, A. J. Ferguson, D. Zhao, K. Wijeratne, A. Wurger, J. L. Blackburn, X. Crispin and S. Fabiano, *Chem. Rev.*, 2021, **121**, 12465.
4 H. Zhu, T. Zhao, B. Zhang, Z. An, S. Mao, G. Wang, X. Han, X. Lu, J. Zhang and X. Zhou, *Adv. Energy Mater.*, 2020, **11**, 2003304.
5 S. He, S. Lehmann, A. Bahrami and K. Nielsch, *Adv. Energy Mater.*, 2021, **11**, 2101877.
6 M. N. Hasan, H. Wahid, N. Nayan and M. S. Mohamed Ali, *Int. J. Energy Res.*, 2020, **44**, 6170.
7 C. Jiang, P. Wei, Y. Ding, K. Cai, L. Tong, Q. Gao, Y. Lu, W. Zhao and S. Chen, *Nano Energy*, 2021, **80**, 105488.
8 G. Prunet, F. Pawula, G. Fleury, E. Cloutet, A. J. Robinson, G. Hadziioannou and A. Pakdel, *Mater. Today Phys.*, 2021, **18**, 100402.
9 S. Masoumi, S. O'Shaughnessy and A. Pakdel, *Nano Energy*, 2022, **92**, 106774.
10 Q. Jiang, X. Lan, C. Liu, H. Shi, Z. Zhu, F. Zhao, J. Xu and F. Jiang, *Mater. Chem. Front.*, 2018, **2**, 679.
11 Y. Zhang, W. Wang, F. Zhang, K. Dai, C. Li, Y. Fan, G. Chen and Q. Zheng, *Small*, 2022, **18**, e2104922.
12 Y. Wang, L. Yang, X. L. Shi, X. Shi, L. Chen, M. S. Dargusch, J. Zou and Z. G. Chen, *Adv. Funct. Mater.*, 2019, **31**, 1807916.
13 N. Bisht, P. More, P. K. Khanna, R. Abolhassani, Y. K. Mishra and M. Madsen, *Adv. Mater.*, 2021, **2**, 1927.
14 C. Liu, D.-L. Shan, Z.-H. Shen, G.-K. Ren, W. Yue, Z.-F. Zhou, J.-Y. Li, D. Yi, J.-L. Lan, L.-Q. Chen, G. J. Snyder, Y.-H. Lin and C.-W. Nan, *Nano Energy*, 2021, **89**, 106380.
15 K. Yusupov and A. Vomiero, *Adv. Funct. Mater.*, 2020, **30**, 2002015.
16 Z. Liu and G. Chen, *Adv. Mater. Technol.*, 2020, **5**, 2000049.
17 H. Yao, Z. Fan, H. Cheng, X. Guan, C. Wang, K. Sun and J. Ouyang, *Macromol. Rapid Commun.*, 2018, **39**, 1700727.
18 M. Goel and M. Thelakkat, *Macromolecules*, 2020, **53**, 3632.
19 M. Statz, S. Schneider, F. J. Berger, L. Lai, W. A. Wood, M. Abdi-Jalebi, S. Leingang, H. J. Himmel, J. Zaumseil and H. Sirringhaus, *ACS Nano*, 2020, **14**, 15552.

20 H. Song, Y. Qiu, Y. Wang, K. Cai, D. Li, Y. Deng and J. He, *Compos. Sci. Technol.*, 2017, **153**, 71.
21 N. Nandihalli, C.-J. Liu and T. Mori, *Nano Energy*, 2020, **78**, 105186.
22 Y. Zhang, Q. Zhang and G. Chen, *Carbon Energy*, 2020, **2**, 408.
23 Y. Wang, Z. Chen, H. Huang, D. Wang, D. Liu and L. Wang, *J. Mater. Chem. A*, 2020, **8**, 24675.
24 Y. Yang, H. Deng and Q. Fu, *Mater. Chem. Front.*, 2020, **4**, 3130.
25 S. H. Kim, S. Jeong, D. Kim, C. Y. Son and K. Cho, *Adv. Electron. Mater.*, 2023, **9**, 2210293.
26 J. Liang, R. Cui, X. Zhang, K. Koumoto and C. Wan, *Adv. Funct. Mater.*, 2022, **33**, 2208813.
27 T. Rodrigues-Marinho, V. Correia, C. R. Tubio, A. Ares-Pernas, M. J. Abad, S. Lanceros-Méndez and P. Costa, *Chem. Eng. J.*, 2023, **473**, 145297.
28 B. Xu, T. Feng, Z. Li, W. Zheng and Y. Wu, *Adv. Funct. Mater.*, 2018, **30**, e1801904.
29 S. Liu, H. Li, J. C. C. Yeo, J. Kong, P. Anukunwithaya and C. He, *Carbon*, 2023, **203**, 111.
30 Y. H. Kang, U.-H. Lee, I. H. Jung, S. C. Yoon and S. Y. Cho, *ACS Appl. Electron. Mater.*, 2019, **1**, 1282.
31 D. Kim, Y. Park, D. Ju, G. Lee, W. Kwon and K. Cho, *Chem. Mater.*, 2021, **33**, 4853.
32 T. Wan, X. Yin, C. Pan, D. Liu, X. Zhou, C. Gao, W. Y. Wong and L. Wang, *Polymer*, 2019, **11**, 593.
33 H. Zhou, X. Li, C. Gao, F. Yang, X. Ye, Y. Liu and L. Wang, *Compos. Sci. Technol.*, 2021, **201**, 108518.
34 L. Wang, C. Pan, Z. Chen, W. Zhou, C. Gao and L. Wang, *ACS Appl. Energy Mater.*, 2018, **1**, 5075.
35 Z. Chen, M. Lai, L. Cai, W. Zhou, D. Xie, C. Pan and Y. Qiu, *Polymer*, 2020, **12**, 1447.
36 X. Zhou, C. Pan, A. Liang, L. Wang and W.-Y. Wong, *Compos. Sci. Technol.*, 2017, **145**, 40.
37 J. Jung, E. H. Suh, Y. J. Jeong, H. S. Yang, T. Lee and J. Jang, *ACS Appl. Mater. Interfaces*, 2019, **11**, 47330.
38 P.-S. Lin, S. Inagaki, J.-H. Liu, M.-C. Chen, T. Higashihara and C.-L. Liu, *Chem. Eng. J.*, 2023, **458**, 141366.
39 J. H. Koo, D. C. Kim, H. J. Shim, T.-H. Kim and D.-H. Kim, *Adv. Funct. Mater.*, 2018, **28**, 1801834.
40 S. Wang, J. Xu, W. Wang, G. N. Wang, R. Rastak, F. Molina-Lopez, J. W. Chung, S. Niu, V. R. Feig, J. Lopez, T. Lei, S. K. Kwon, Y. Kim, A. M. Foudeh, A. Ehrlich, A. Gasperini, Y. Yun, B. Murmann, J. B. Tok and Z. Bao, *Nature*, 2018, **555**, 83.
41 X. Fan, W. Nie, H. Tsai, N. Wang, H. Huang, Y. Cheng, R. Wen, L. Ma, F. Yan and Y. Xia, *Adv. Sci.*, 2019, **6**, 1900813.
42 S. J. Benight, C. Wang, J. B. H. Tok and Z. Bao, *Prog. Polym. Sci.*, 2013, **38**, 1961.
43 Y. Jia, Q. Jiang, H. Sun, P. Liu, D. Hu, Y. Pei, W. Liu, X. Crispin, S. Fabiano, Y. Ma and Y. Cao, *Adv. Funct. Mater.*, 2021, **33**, 2102990.
44 Y. Huang, C. Peng, Y. Li, Y. Yang and W. Feng, *Aggregate*, 2023, **4**, e319.
45 E. W. Zaia, M. P. Gordon, P. Yuan and J. J. Urban, *Adv. Electron. Mater.*, 2019, **5**, 1800823.
46 Y. Hao, X. He, L. Wang, X. Qin, G. Chen and J. Yu, *Adv. Funct. Mater.*, 2021, **32**, 2109790.
47 C. Zhang, Q. Zhang, D. Zhang, M. Wang, Y. Bo, X. Fan, F. Li, J. Liang, Y. Huang, R. Ma and Y. Chen, *Nano Lett.*, 2021, **21**, 1047.
48 X. He, J. Shi, Y. Hao, L. Wang, X. Qin and J. Yu, *Compos. Commun.*, 2021, **27**, 100822.
49 L. Liang, C. Gao, G. Chen and C.-Y. Guo, *J. Mater. Chem. C*, 2016, **4**, 526–532.
50 L. Xu, W. Wang, L. Zhang, D. Wang and A. Zhang, *ACS Appl. Mater. Interfaces*, 2022, **14**, 21623.
51 Y. Wang, Z. Zhou, J. Zhou, L. Shao, Y. Wang and Y. Deng, *Adv. Energy Mater.*, 2021, **12**, 2102835.
52 W.-W. Liang, Y.-S. Lin, Y.-Y. Lai and Y.-J. Cheng, *React. Funct. Polym.*, 2016, **108**, 113.
53 S. Pan, Z. Pei, Z. Jing, J. Song, W. Zhang, Q. Zhang and S. Sang, *RSC Adv.*, 2020, **10**, 11225.
54 A. Mohapatra, A. Singh, S. A. Abbas, Y.-J. Lu, K. M. Boopathi, C. Hanmandlu, N. Kaisar, C.-H. Lee and C.-W. Chu, *Nano Energy*, 2019, **63**, 103826.
55 F. Liu, G. L. Espejo, S. Qiu, M. M. Oliva, J. Pina, J. S. Seixas de Melo, J. Casado and X. Zhu, *J. Am. Chem. Soc.*, 2015, **137**, 10357–10366.
56 F. Liu, Z. Zhou, C. Zhang, T. Vergote, H. Fan, F. Liu and X. Zhu, *J. Am. Chem. Soc.*, 2016, **138**, 15523–15526.
57 T. H. Kim and J. I. Hong, *ACS Appl. Mater. Interfaces*, 2022, **14**, 55627.
58 R. Niu, C. Pan, Z. Chen, L. Wang and L. Wang, *Chem. Eng. J.*, 2020, **381**, 122650.
59 G. Cao, G. He, L. Lu, Q. Zhang, Y. Yan, X. Tang, J. Wu, S. Wang, L. Wang and C. Gao, *Chem. Eng. J.*, 2023, **474**, 145664.
60 N. Kim, S. Lienemann, I. Petsagkourakis, D. Alemu Mengistie, S. Kee, T. Ederth, V. Gueskine, P. Leclere, R. Lazzaroni, X. Crispin and K. Tybrandt, *Nat. Commun.*, 2020, **11**, 1424.
61 Z. Peng, K. Xian, Y. Cui, Q. Qi, J. Liu, Y. Xu, Y. Chai, C. Yang, J. Hou, Y. Geng and L. Ye, *Adv. Funct. Mater.*, 2021, **33**, 2106732.
62 K.-H. Jeon and J.-W. Park, *Macromolecules*, 2022, **55**, 8311.